ACS NANO

www.acsnano.org

ARTICLE

# The Interplay of Polymer Bridging and Entanglement in Toughening Polymer-Infiltrated Nanoparticle Films

Yiwei Qiang, Sumukh S. Pande, Daeyeon Lee,* and Kevin T. Turner*

Cite This: *ACS Nano* 2022, 16, 6372−6381

Read Online

ACCESS | Metrics & More | Article Recommendations | Supporting Information

**ABSTRACT:** **Polymer-nanoparticle composite films (PNCFs) with high loadings of nanoparticles (NPs) (>50 vol %) have applications in multiple areas, and an understanding of their mechanical properties is essential for their broader use. The high-volume fraction and small size of the NPs lead to physical confinement of the polymers that can drastically change the properties of polymers relative to the bulk. We investigate the fracture behavior of a class of highly loaded PNCFs prepared by polymer infiltration into NP packings. These polymer-infiltrated nanoparticle films (PINFs) have applications as multifunctional coatings and membranes and provide a platform to understand the behavior of polymers that are highly confined. Here, the extent of confinement in PINFs is tuned from 0.1 to 44 and the fracture toughness of PINFs is increased by up to a factor of 12 by varying the molecular weight of the polymers over 3 orders of magnitude and using NPs with diameters ranging from 9 to 100 nm. The results show that brittle, low molecular weight (MW) polymers can significantly toughen NP packings, and this toughening effect becomes less pronounced with increasing NP size. In contrast, high MW polymers capable of forming interchain entanglements are more effective in toughening large NP packings. We propose that confinement has competing effects of polymer bridging increasing toughness and chain disentanglement decreasing toughness. These findings provide insight into the fracture behavior of confined polymers and will guide the development of mechanically robust PINFs as well as other highly loaded PNCFs.**

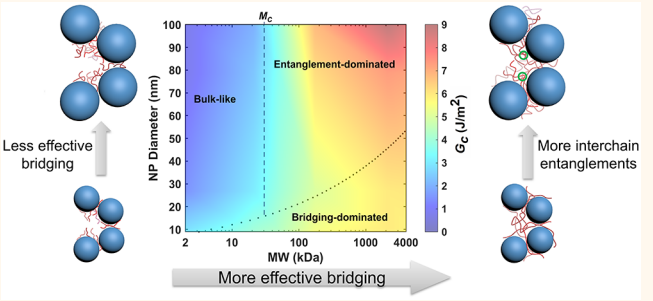


**KEYWORDS:** *polymer-nanoparticle composite films, confinement, double cantilever beam, confinement-induced molecular bridging, polymer entanglement*



Polymer-nanoparticle composite films (PNCFs) are a class of hybrid materials that synergistically combine the functionality of nanoparticles (NPs) and the flexibility and processability of polymers.[1] Recently, highly loaded PNCFs with a NP fraction >50 vol % have been shown to have transport and mechanical properties that are superior to their counterparts with low NP fractions.[2,3] For example, nacre-mimetic PNCFs, composed of a large volume fraction of plate-like NPs and a small fraction of polymers, not only show exceptional strength and toughness but also have properties that allow for their use in flame-retardant and gas barrier applications.[4−7] PNCFs with a high loading of conductive NPs, such as indium tin oxide and boron nitride, are attractive for applications where high thermal or electrical conductivity is desired.[8−11]

One important feature in highly loaded PNCFs is that the size of the spaces between the NPs can be comparable to or smaller than the characteristic size of the polymers in their unperturbed state, resulting in significant confinement of the polymer chains. Confinement effects are also observed in other polymer nanocomposites (PNCs), polymeric thin films, and biological systems.[12−15] Polymer chains in a confined space have to adopt conformational changes to reduce the volume pervaded by each chain.[16,17] Highly confined polymers can have drastically different physicochemical[16,18−20] and mechanical properties[21−26] from their bulk counterparts. For example, molecular dynamics simulations of nacre-inspired nanocomposites have shown that confinement leads to a 2−6-fold increase in the elastic modulus of the polymer phase.[25] However, confinement has been also found to decrease the

Received: January 14, 2022
Accepted: March 30, 2022
Published: April 5, 2022

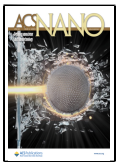

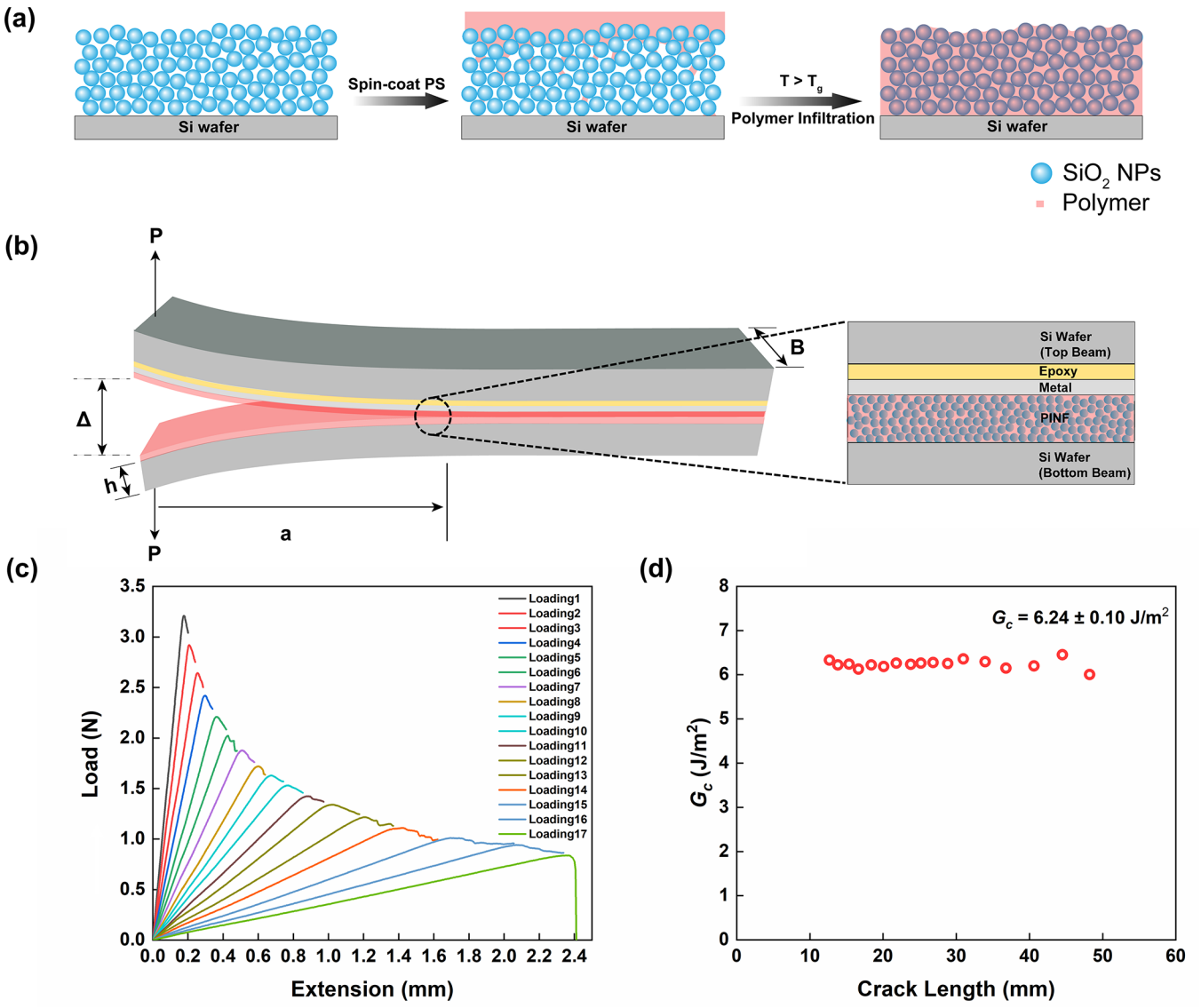


**Figure 1.** (a) Schematic showing the preparation of a PINF by spin coating PS atop a densely packed NP layer and infiltrating PS into the voids of NP layer via capillarity. (b) Schematic of the DCB specimen used to measure the fracture toughness of PINFs. The relative thicknesses of each layer are not drawn to scale. (c) Representative load−displacement curves for a DCB test of a PINF (NP diameter = 79 nm, MW = 173,000 g mol$^{-1}$). Multiple loading/crack-growth/unloading cycles are performed to obtain $G_c$ at different crack lengths yielding the crack growth resistance curve shown in (d).

strength of PNCFs due to a reduction of entanglement density.[23] As entanglements are the fundamental mechanism behind high fracture toughness in bulk polymers, highly loaded PNCFs tend to be brittle, potentially limiting their performance and durability in practical applications.[2,27] Thus, there is a critical need to understand the effect of confinement on the fracture behavior of PNCFs with high fractions of NPs. Compared to extensively studied neat polymer films and PNCFs with low fractions of NPs,[21,22,28−31] there are relatively few systematic studies addressing the impact of confinement on the fracture properties of highly loaded PNCFs. Experimental investigations have been hampered by the ability to prepare highly loaded PNCFs with controlled degrees of confinement[32−34] as well as challenges in measuring the fracture properties of thin films.

In this work, we investigate the effect of polymer chain confinement on the fracture behavior of composites consisting of dense packings of silica NPs infiltrated with a glassy polymer, polystyrene. These highly loaded composites are prepared by a recently developed capillary rise infiltration (CaRI) technique, which takes advantage of capillarity-induced imbibition of polymer into the interstices of dense packings of NPs.[35−38] This method overcomes the difficulties associated with mixing and stabilizing a large amount of nanofillers in a polymer matrix using conventional methods such as solution mixing or melt compounding.[2,11,34,39] CaRI has been applied to a wide range of polymers and NPs[40,41] and enables the fabrication of PINFs for various applications including Bragg reflector sensors,[42] oil/water separation,[43,44] and anticorrosive coatings.[45] Moreover, CaRI is a powerful approach to fabricate materials that can be used to investigate polymer behavior under extreme confinement. The characteristic pore size in random close packings of spheres is approximately 30% of the NP size.[46] Thus, it is straightforward to tune the degree of confinement by changing NP size and/or the molecular weight of the polymer. In previous work, the CaRI system has been


https://doi.org/10.1021/acsnano.2c00471
ACS Nano 2022, 16, 6372−6381

used to show that the transport and thermal properties of polymers can drastically deviate from the bulk due to the effect of confinement.[33,47−49]

Although the fracture toughness of polymer-infiltrated nanoparticle films (PINFs) prepared by CaRI has been previously measured with a nanoindentation-based pillar-splitting method, the underlying toughening mechanisms and the role of confinement are not well understood.[50] Here, we use a thin-film fracture testing method based on the double cantilever beam (DCB) specimen to achieve highly accurate measurements of the fracture toughness of PINFs in mode I (tensile crack opening). The extent of confinement is tuned over a wide range by using PS with molecular weights (MWs) that span three orders of magnitude and $SiO_2$ NPs with four different diameters between 9 and 100 nm. We demonstrate that polymers can significantly toughen NP films even when they are under extreme confinement and completely lose interchain entanglement. We also show that low MW polymers are more effective in toughening small NP packings, whereas high MW polymers result in greater toughening in packings comprised of large NPs. The results suggest that both confinement-induced molecular bridging and chain entanglement contribute to toughening PINFs and the relative importance of the two mechanisms is dependent on the extent of confinement.

## RESULTS AND DISCUSSION

We investigate the fracture behavior of a highly loaded PNCFs prepared by polymer infiltration into NP packings. Polystyrene (PS) is infiltrated into the NP packings by heating a bilayer film composed of a PS film atop a densely packed $SiO_2$ NP layer (packing fraction ~65 vol %) above the glass transition temperature ($T_g$) of PS (Figure 1a and Figure S2). Polymer chains experience strong physical confinement imposed by the NPs.[33,47] We tune the degree of confinement by varying the PS molecular weight (MW) and $SiO_2$ NP size. Polymers with six different MWs, spanning three orders of magnitude, are used, including both unentangled (2k and 21k) and entangled PS (51k, 173k, 2.1 M and 4M). The radius of gyration ($R_g$) of PS, calculated based on the Kuhn length of PS (1.8 nm),[51] ranges from 1.2 to 54.8 nm. $SiO_2$ NPs with diameters ranging from 9 to 100 nm are used as shown in Figure S1. Given that the average pore radius ($R_{pore}$) in a disordered packing of spherical NPs is approximately 29% of the particle radius,[46] $R_{pore}$ varies from 1.2 to 14.5 nm. To estimate the degree of confinement, we define a confinement ratio (CR), as the ratio between the radius of gyration of unperturbed polymer chain ($R_g$) and average pore radius (i.e., CR = $R_g/R_{pore}$). With the polymers and NPs used in this work, CR varies from 0.1 to 44 as listed in Table S1.

To quantitatively probe the fracture behavior of PINFs, we use a thin-film fracture testing method based on the DCB specimen. All PINFs have thicknesses of ~250 nm (see Supporting Information for detailed characterization). Neat NP and polymer films are also tested. As depicted in Figure 1b, a DCB specimen is fabricated by constructing a multilayer stack composed of Si/epoxy/metal layer/testing film/Si. The specimen is loaded in the displacement control, and the load−displacement data are continuously recorded. Figure 1c shows typical load−displacement curves from the DCB test on a PINF (NP diameter = 79 nm, MW = 173,000 g $mol^{-1}$) where cohesive fracture within the PINF is verified by ellipsometry and scanning electron microscopy (SEM). The specimen is initially loaded elastically, but once the strain energy release rate ($G$) exceeds the critical strain energy release rate (i.e., toughness $G_c$) of the PINF, a crack propagates in the PINF. After the crack grows for several millimeters, the specimen is unloaded and then subjected to multiple loading/crack-growth/unloading cycles until complete fracture. In this manner, between 10 and 20 independent measurements of $G_c$ over crack lengths from about 10 to 50 mm are collected from a single DCB specimen. $G_c$ calculated for different crack lengths (see Materials and Methods for detailed information) is shown in Figure 1d. The relatively constant $G_c$ (6.24 ± 0.10 $J/m^2$) at different crack lengths along with the smooth load−displacement curves indicate stable crack propagation through PINFs over distances of tens of millimeters, demonstrating the high reliability of this method for characterizing the fracture toughness of PINFs. We note that PINFs are free of large defects like aggregates and the interstitial voids are nearly completely filled with polymers. Therefore, defects are expected to have little effect on the fracture behavior of PINFs since the defect size or population is not expected to change with polymer MW or NP size.

Figure 2 shows the $G_c$ of PINFs with different NP size as a function of polymer MW. All PINFs show significantly high $G_c$

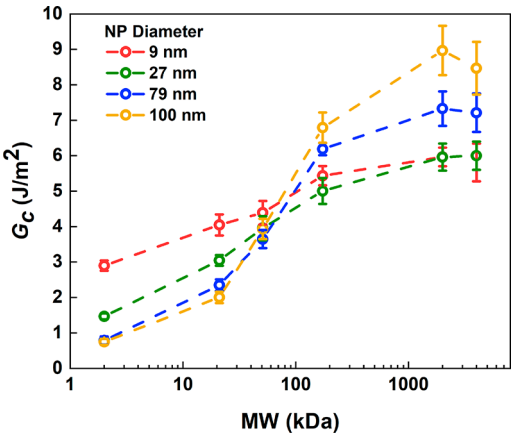


**Figure 2. $G_c$ as a function of polymer MW for PINFs with different NP diameters.**

than neat NP films which have very weak inter-NP cohesion (Figure S6). For example, neat 9 nm NP films have a $G_c$ of 1.2 $J/m^2$. When 2k PS ($R_g$ = 1.2 nm) infiltrates into the NP films, $G_c$ increases to 2.9 $J/m^2$. Such enhancement in $G_c$ is significant considering the brittle nature of neat 2k PS, which has a $G_c$ of 0.3 $J/m^2$ (Figure S7). With increasing MW, $G_c$ of PINFs with 9 nm NPs increases further and reaches a plateau of ~6 $J/m^2$ at a MW of approximately 2M. We observe a similar trend of increasing $G_c$ with MW before reaching a plateau at high MW for PINFs with various NP diameters. The plateau values increase from ~6 $J/m^2$ for PINFs composed of 9 nm NPs to ~8.5 $J/m^2$ for PINFs composed of 100 nm NPs.

Although the MW dependence of $G_c$ observed for PINFs is similar to that of neat polymers (Figure S7), the underlying mechanisms leading to this behavior are very different. In neat glassy polymers, such as PS, polymer fracture transitions from segment pullout below the critical entanglement MW, $M_e$ (for PS, $M_e$ = 31,000 g $mol^{-1}$) to crazing above $M_e$.[27,52] Crazing is a plastic deformation process and leads to a significantly higher $G_c$ for entangled polymers than that for unentangled


https://doi.org/10.1021/acsnano.2c00471
ACS Nano 2022, 16, 6372−6381

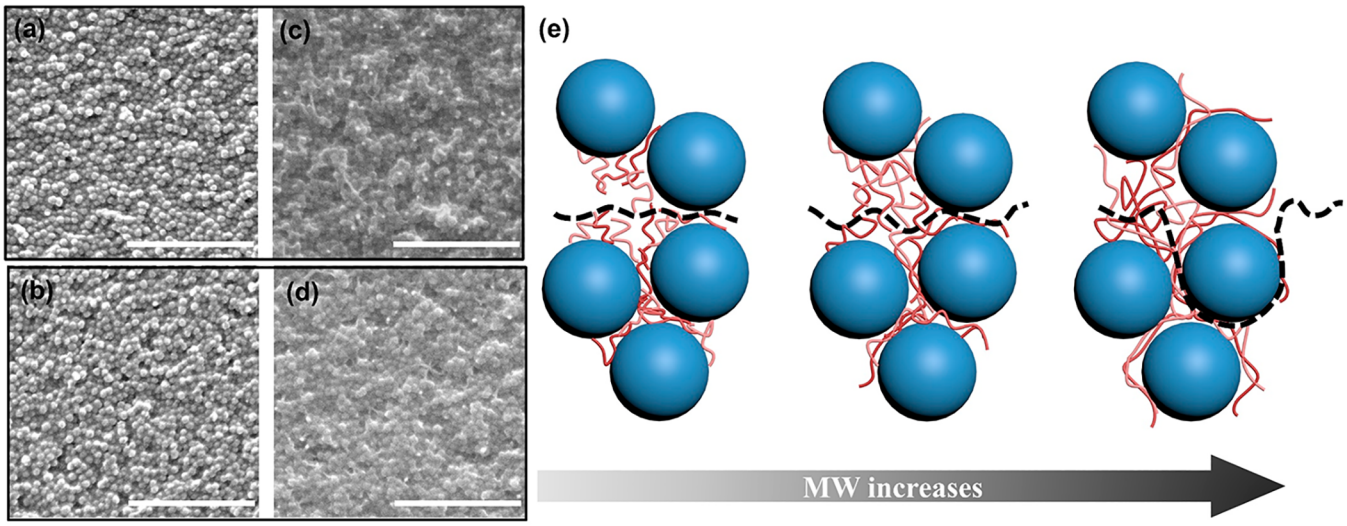


**Figure 3. SEM images of the fractured surfaces of NP ($D$ = 27 nm) films infiltrated with (a, b) 2k PS and (c, d) 2.1M PS. The (b) and (d) images are taken from the bottom beams where PINFs are initially deposited on, while (a) and (c) are taken from the top beams. All scale bars are 500 nm. (e) Schematic illustration of the crack path (black dashed line) in PINFs ($D$ = 27 nm). As the polymer MW increases, the crack path becomes more tortuous with more NPs and polymers pulled out from the bottom beams to the top beams.**

polymers.[53] As MW increases, the size of the craze deformation zone increases and more energy is dissipated during fracture.[27,54] The fractured surfaces typically show increasing roughness with MW and evidence of local plastic deformation in entangled polymers (Figure S8).[55,56]

Such entanglement-induced toughening, however, is unlikely to be the dominant mechanism when polymers are strongly confined in NP packings. In fact, in our most highly confined systems, that is, PINFs composed of 9 nm NPs, we observe similar fracture surfaces regardless of polymer MW and no evidence of local plastic deformation (Figure S9). Recent molecular dynamics simulations have shown that the average entanglement length of polymers in PINFs increases compared to bulk, corresponding to a decrease in entanglement density.[57] Entanglement reduction has been widely reported for polymers under thin-film and cylindrical confinement as well as in other PNCs.[14,17,58,59] In PNCs, the interchain entanglement density decreases with increasing NP loadings and vanishes at high NP loadings.[58,59] Thus, we expect significant reduction of interchain entanglements in PINFs as the NP loadings reach the random-close-packing limit (~65 vol %). Scaling arguments have also shown that polymers in cylindrical pores can be completely disentangled under hyper-confinement. The critical MW at the onset of hyper-confinement, $M_{c,\text{hyper-confinement}}$, can be calculated as[60−62]

$$M_{c,\text{hyper-confinement}} = N_c \times M_o = \left(\frac{d_{\text{pore}}}{b}\right)^4 \times M_o \quad (1)$$

where $N_c$ is number of Kuhn monomers at the onset of hyper-confinement, $M_o$ is the molar mass of a Kuhn monomer (720 g mol$^{-1}$ for PS), and $b$ is the Kuhn length of the polymer (1.8 nm for PS).[51] We calculate the onset of hyper-confinement in PINFs with different pore sizes (Table S1), although the pore geometry in PINFs is different from cylindrical pores. The $M_{c,\text{hyper-confinement}}$ of PS in 9 and 27 nm packings is 2 kDa and 254 kDa, respectively. Thus, high MW PS used in this study are under or close to hyper-confinement in these two packings. In addition, even if interchain entanglements exist in these two packings, the load transfer between the chains is limited due to the surrounding NPs. These arguments suggest that interchain entanglements play little role in toughening the small (9 and 27 nm) NP packings.

An alternative toughening mechanism in PINFs with small NPs is confinement-induced molecular bridging, which was previously proposed for polymers confined in a porous organosilicate matrix.[61−63] In this mechanism, polymer chains near the crack front bridge the surfaces of the crack and are pulled out from the pores as the crack propagates. The frictional pullout and elongation of many individual polymer chains dissipate energy and toughen the composite. Polymers with higher MW have longer chains and are pulled out over longer distances, and thus dissipate more energy. This mechanism is ultimately limited by the strength of polymer backbone and results in a plateau of $G_c$ at high MW, consistent with the experimental measurements in Figure 2.

The confinement-induced molecular bridging mechanism is supported by the MW dependence of $G_c$ shown in Figure 2 as well as the SEM images of the fractured surfaces in PINFs composed of 27 nm NPs shown in Figure 3. The crack is driven off the centerline toward the PINFs−metal interface due to lower elastic modulus of the PINFs compared to the substrates.[64] As the interface is strongly bonded, fracture occurs below the topmost NP layer and the underlying NP layer which is confirmed by ellipsometry. When 2k PS ($R_g$ = 1.2 nm) is infiltrated into the 27 nm NP packings, these short polymer chains can only bridge neighboring NPs (Figure 3e). Only the topmost NP layer and a small number of the underlying NP layer are found on the top beams (Figure 3a). Similar fracture surfaces are observed in PINFs with 21k and 51k PS. In contrast, more NPs are found on the top beams with higher MW polymers such as 2.1M ($R_g$ = 39.7 nm) (Figure 3c). Recent molecular dynamics simulations have confirmed that polymer chains confined in NP packings adopt bulk-like conformation below entanglement MW[65] and more stretched conformation above entanglement MW.[57] High MW polymers stretch over large distances and bridge more than neighboring NPs (see SI for detailed discussion). As a result, more NPs are pulled out along with the polymer chains from


https://doi.org/10.1021/acsnano.2c00471
ACS Nano 2022, 16, 6372−6381

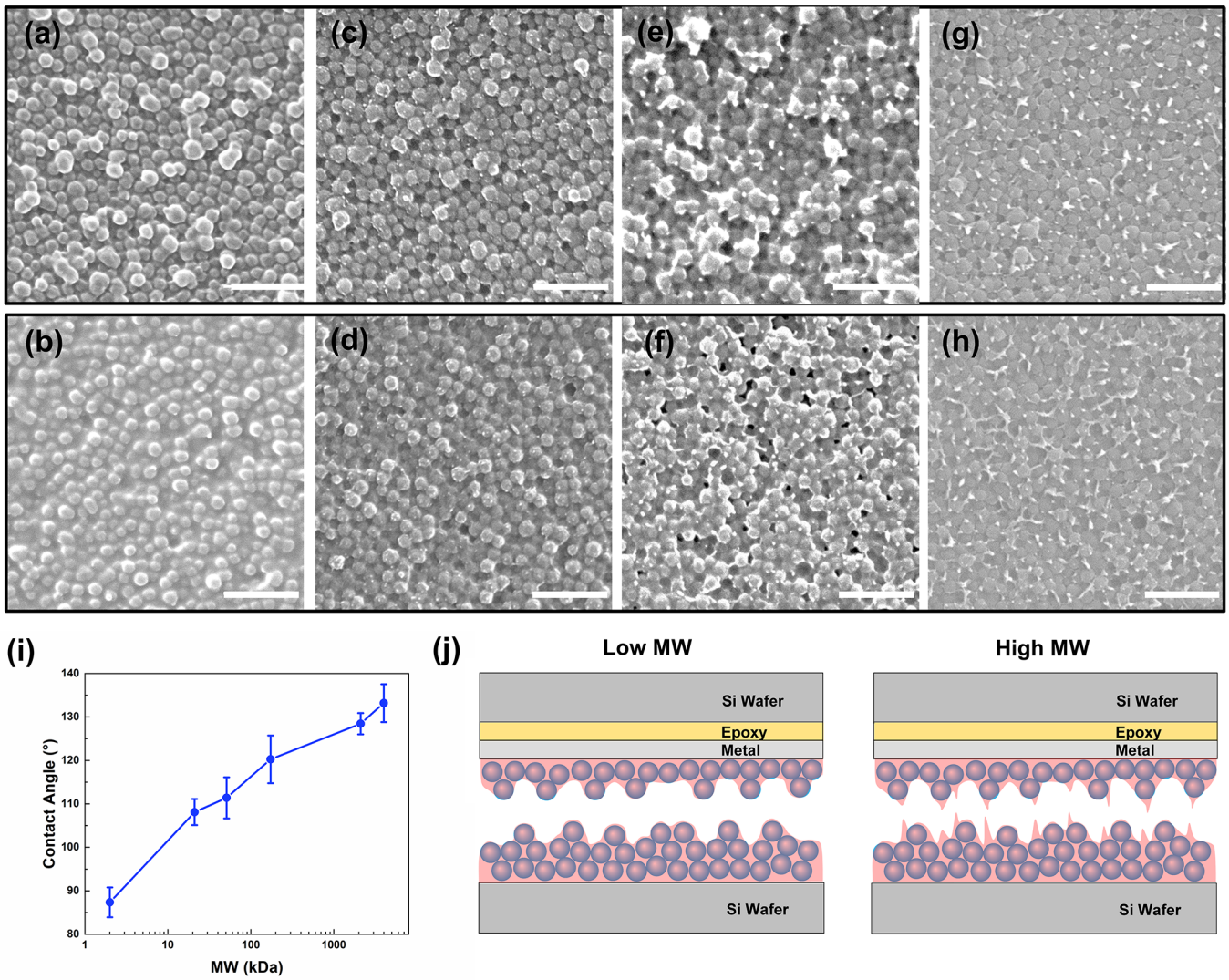


**Figure 4. SEM images of the fractured surfaces of NP ($D$ = 79 nm) films infiltrated with (a, b) 2k PS, (c, d) 21k PS, (e, f) 51k PS, and (g, h) 173k PS. The (b), (d), (f), and (h) images are taken from the bottom beams where PINFs are initially deposited on, while (a), (c), (e), and (g) are taken from top beams. All scale bars are 500 nm. (i) Water contact angle on the fractured surfaces of PINFs ($D$ = 79 nm). (j) Schematic illustration of the fractured surfaces. PINFs filled with high MW PS show fractured surfaces with protruding polymer filaments compared to those filled with low MW PS.**

the bottom beams to the top beams as illustrated in Figure 3e. We note that unlike in other confinement geometries, such as cylindrical geometries where polymer chains are oriented along the pore axis,[66] we believe that the polymer chains can orient in all directions and bridge NPs isotropically due to interconnected pore geometry in NP packings.

Although chain entanglement plays a negligible role in toughening the 9 and 27 nm packings, it gains importance as NP size increases (i.e., CR decreases). High MW polymer chains such as 173k PS are substantially less confined in 79 nm (CR = 1) and 100 nm NP (CR = 0.8) packings than in 9 nm (CR = 2.9) and 27 nm NP (CR = 9.1) packings. The pore diameters in these large NP packings are much larger than the chain segments ($D_{pore} \gg b$), and polymers cannot be hyper-confined in the molecular-weight range that we use in this study (Table S1). Thus, polymers in these packings are unlikely to be fully disentangled. We observe evidence of chain entanglement from the SEM images of the fractured surfaces (Figure 4). In the PINFs with 79 nm NPs and unentangled 2k PS, NPs appear to be covered with polymers, suggesting that the crack propagates through polymers by pullout of the short chains. When MW increases to 21k, grain-like features appear on the fractured surfaces, consistent with neat 21k PS films (Figure S7). Water contact angle measurements on the fractured surfaces increase significantly from ~87° for 2k infiltrated films to ~110° in 21k infiltrated films (Figure 4i). Considering the hydrophobic nature of PS (water contact angle ~93°), this indicates rougher surfaces are present likely due to pullout of longer chains. The water contact angle of the surfaces further increases with higher polymer MW and reaches up to ~130° at a MW of 2.1M. Interchain entanglements of these high MW polymers enable stress transfer between the chains and induce local plastic deformation, leading to rougher surfaces, as schematically illustrated in Figure 4j.

To better understand the interplay between polymer bridging and entanglement in toughening NP packings, $G_c$ is shown as a function of NP size in Figure 5a. We note that the $G_c$ of neat NP films also depends on the particle size, as shown in Figure S6. The neat NP films are tested under ambient


https://doi.org/10.1021/acsnano.2c00471
ACS Nano 2022, 16, 6372−6381

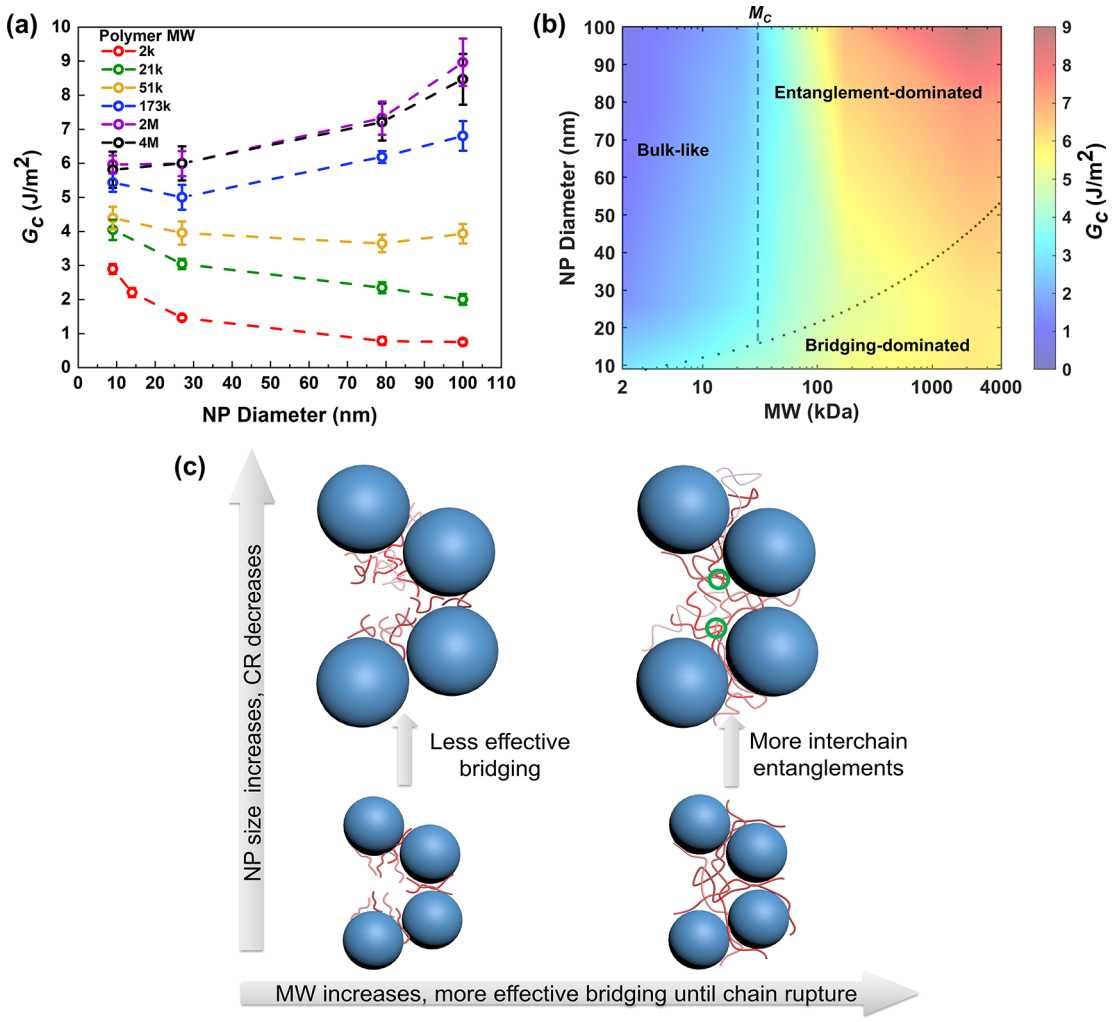


**Figure 5.** (a) $G_c$ as a function of NP diameter for PINFs with different polymer MW. (b) A map showing $G_c$ as a function of polymer MW and NP diameter and corresponding toughening mechanisms. The dashed line marks the critical entanglement MW ($M_c$) of PS and the dotted line marks the onset of hyper-confinement calculated based on eq 1. (c) Schematic illustration of the toughening mechanisms in PINFs. Polymers bridge NPs more effectively as MW increases. Confinement-induced molecular bridging mechanism is dominant in small NP packings, while polymer entanglement plays an important role in large NP packings. Interchain entanglements are highlighted in green circles.

conditions in which capillary forces at the NP junctions can contribute to the mechanical response. The capillary interactions play a larger role in determining $G_c$ of neat NPs than van der Waals forces.[67,68] As water bridges are replaced with polymer bridges in PINFs, we expect that the $G_c$ of PINFs is primarily determined by the polymers and that the contribution from van der Waals interactions between NPs is small. The data in Figure 5a show that there are different trends with NP size when low MW or high MW polymers are used. Low MW polymers, such as 2k and 21k PS, toughen small NP packings more effectively than large NP packings. For example, 2k PS-infiltrated 9 nm NP packings are ~4 times tougher than 2k PS-infiltrated 100 nm packings. Since these polymers are too short to form entanglements, they can only toughen NP packings through confinement-induced molecular bridging. As shown in Figure 5b,c, with increasing NP size, the bridging effect becomes less pronounced, and polymers behave in a more bulk-like manner, consistent with previous studies on the fracture behavior of oligomer-filled organosilicate nanoporous network and the molecular strength-limited bridging model where energy dissipation by bridging effect is predicted to be inversely proportional to pore diameter.[61,63] With increasing NP size, the $G_c$ of PINFs with low MW PS gradually approaches that of neat PS films (0.32 J/m$^2$ for 2k and 1.35 J/m$^2$ for 21k) but remains slightly larger due to a more tortuous crack path. In contrast, high MW polymers such as 2.1M PS show enhanced toughening in large NP packings. High MW polymers also experience less confinement as NP size increases; however, interchain entanglements allow chains to better sustain stress before the polymer backbone ruptures, hence more energy is dissipated. The $G_c$ of PINFs with high MW polymers is lower than bulk PS (Figure S7) due to the reduced entanglement density and limited load transfer with the presence of NPs. The competing effects of confinement on polymer bridging and entanglement result in a relatively constant $G_c$ of ~4 J/m$^2$ for PINFs infiltrated with 51k PS, close to that of neat 51k PS (4.2 J/m$^2$).

## CONCLUSIONS

Our results provide an understanding of the role of polymer confinement on the fracture behavior of PINFs. In general, the fracture toughness increases with MW regardless of NP size.



https://doi.org/10.1021/acsnano.2c00471
ACS Nano 2022, 16, 6372−6381

Low MW polymers toughen small NP packings more effectively, whereas high MW polymers show enhanced toughening in large NP packings. We attribute this difference to changes in polymer conformation and entanglement density due to extreme nanoconfinement and propose two possible toughening mechanisms: confinement-induced molecular bridging and polymer entanglement. The former mechanism is dominant in small NP packings where polymers lose interchain entanglement and adopt extended conformation. As CR decreases, the bridging mechanism becomes less pronounced, and polymer interchain entanglements toughen the PINFs. These results provide guidance for the design of damage-tolerant PINFs and other highly loaded PNCFs with improved fracture resistance, which can be advantageous for applications such as filtration membranes and structural coatings.

## MATERIALS AND METHODS

**Materials.** Polystyrene (PS) of six different molecular weights (2k PS, $M_n$ = 2000 g mol$^{-1}$, PDI = 1.09; 21k PS, $M_n$ = 21,000 g mol$^{-1}$, PDI = 1.04; 51k PS, $M_n$ = 51,000 g mol$^{-1}$, PDI = 1.03; 173k PS, $M_n$ = 173,000 g mol$^{-1}$, PDI = 1.06; 2.1M PS, $M_n$ = 2,100,000 g mol$^{-1}$, PDI = 1.15; 4M PS, $M_n$ = 4,049,000 g mol$^{-1}$, PDI = 1.09) is purchased from Polymer Source, Inc. Silica ($SiO_2$) NPs with diameters of 9 nm (LUDOX SM-30, 30 wt % suspension in water), 14 nm (LUDOX HS-30, 30 wt % suspension in water), and 27 nm (LUDOX TM-50, 50 wt % suspension in water) are purchased from Sigma-Aldrich, whereas those with diameters of 79 nm (SNOWTEX ST-YL, 40−41 wt % suspension in water) and 100 nm (SNOWTEX ST-ZL, 40−41 wt % suspension in water) are obtained from Nissan Chemical America Corp. The NP size distribution is determined from the literature[69,70] and scanning electron microscopy (SEM) images (Figure S1).

**Preparation and Characterization of Polymer-Infiltrated Nanoparticle Films.** Prior to film deposition, single-side-polished (100) Si wafers (University Wafer) are rinsed with isopropanol and deionized water, dried with nitrogen, and then treated by oxygen plasma for ∼4 min. To avoid crack formation during polymer infiltration, a PS-top geometry is used, where the NP film is spin-coated first, followed by the PS film.[33] The $SiO_2$ NP suspensions are diluted with deionized $H_2O$ and filtered prior to use (filter pore size 0.45 μm). The filtered NP suspensions are spin-coated onto cleaned Si wafers using a WS-400BZ-6NPP/Lite spin coater from Laurell Technologies Corporation. The concentration of NP suspensions and spin-coating rate are controlled to form a densely packed NP film with a thickness of ∼250 nm. Then, a solution of PS dissolved in toluene is spin-coated onto the NP film to form a bilayer film. The bilayer film is heated at 180°C in a nitrogen-filled oven for 3 h to allow infiltration of PS into the pores of the NP packings (Figure S2). We note that the pores are partially infiltrated with PS during spin coating and the extent of infiltration in this process depends on the size of NPs and the MW of PS. Thus, the concentration of PS solutions and spin-coating rate are carefully controlled such that the pores are nearly completely filled (polymer volume fraction ∼30−35 vol %) after thermal annealing and there is no residual PS layer atop the PINF (Table S3). The thickness and refractive index of deposited films are measured using spectroscopic ellipsometry (Alpha-SE, J.A. Woollam). NP and polymer volume fractions are calculated as previously described.[38] Neat PS and NP films with thicknesses of ∼200 nm are also prepared for fracture tests.

**Fabrication of Double Cantilever Beam Specimens.** The double cantilever beam (DCB) specimens are prepared by first constructing a sandwich structure composed of Si/epoxy/metal/testing film/Si, as depicted in Figure 1a. The metal layer which consists of 25 nm-thick Ti and 100 nm-thick Al layer is deposited on the testing films by magnetron sputtering (Denton Explorer-14). The metal layer acts as a barrier layer to prevent the permeation of epoxy into testing films as well as a stiff elastic standoff layer to prevent plastic deformation of epoxy and associated energy contribution to the fracture toughness of testing films.[71] Afterward, epoxy adhesives (EPO-TEK 353ND, Epoxy Technology, MA) with ∼5 μm thickness are spin-coated onto the metal layer, and a dummy Si wafer is attached to make the sandwich structure. The sandwich structure is then diced with a dicing saw (ADT 7100 Dicing Saw) to create 10 mm-wide DCB specimens.

**Double Cantilever Beam Fracture Testing.** Fracture testing of the DCB specimens was conducted with a MTS test system (Criterion Model 43) fitted with a 50 N load cell. Two loading blocks were attached to the ends of the specimen (Figure S3), and the specimen is loaded in at a constant displacement rate of 1 mm min$^{-1}$. When stable crack propagation is observed, the specimen is unloaded and then reloaded. Multiple loading/crack-growth/unloading cycles are performed until complete fracture of the specimen, and the load-displacement curves are recorded. The crack length, $a$, is calculated based on the compliance of the specimen using[72]

$$a = \left(\frac{CE'Bh^3}{8}\right)^{1/3} - 0.64h \tag{2}$$

where the compliance, $C$, is the inverse slope of the load−displacement curve corrected for machine compliance, $E'$ is the plane-strain modulus of the beam, $B$ is the specimen width, and $h$ is the height of one beam. The critical load, $P_c$, at which crack growth occurs, is the load at which the slope of the load−displacement curve begins to decrease during the loading cycle. The fracture toughness of the film, $G_c$, which is the critical value of applied strain energy release rate, can be calculated by substituting $a$ and $P_c$ into eq 3:

$$G_c = \frac{12P_c^2a^2}{E'B^2h^3}\left(1 + 0.64\frac{h}{a}\right)^2 \tag{3}$$

Multiple values of $G_c$ are obtained for each specimen, and the $G_c$ reported for each sample is the average of $G_c$ of at least three specimens.

**Characterization of Fractured Films.** The thicknesses and refractive indices of the fractured films are measured with an ellipsometer and compared with previously measured unfractured films. When the thickness change is smaller than the diameter of constitutive NPs, adhesive fracture occurs at the PINF−metal interface, and the data are not used. When the thickness change is close to or higher than the diameters of constitutive NPs, the morphologies of fractured films are imaged using a scanning electron microscope (FEI-600 Quanta ESEM) to further examine the crack path. Before imaging, each sample is coated with 4 nm of iridium to prevent charging. The SEM images are captured at an accelerating voltage of 20 kV, a spot size of 3.0, and working distance around 10 mm. The contact angles of water on the fractured films are recorded and analyzed using a Biolin Scientific Attension goniometer.

## ASSOCIATED CONTENT

### Supporting Information

The Supporting Information is available free of charge at https://pubs.acs.org/doi/10.1021/acsnano.2c00471.

Detailed information about NP size, pore size, confinement ratio, and the critical MW at the onset of hyperconfinement; SEM images of neat and polymer-infiltrated NP films; a photograph of the DCB fracture testing setup; ellipsometry measurements of NP films and PINFs; adhesive fracture with residual PS layer; DCB fracture testing results of neat NP and PS films; estimation of confinement-induced molecular bridging effect (PDF)



https://doi.org/10.1021/acsnano.2c00471
ACS Nano 2022, 16, 6372−6381

## AUTHOR INFORMATION


### Corresponding Authors

**Daeyeon Lee** − *Department of Chemical and Biomolecular Engineering, University of Pennsylvania, Philadelphia, Pennsylvania 19104, United States;* orcid.org/0000-0001-6679-290X; Email: daeyeon@seas.upenn.edu

**Kevin T. Turner** − *Department of Mechanical Engineering and Applied Mechanics and Department of Materials Science and Engineering, University of Pennsylvania, Philadelphia, Pennsylvania 19104, United States;* orcid.org/0000-0003-4963-4568; Email: kturner@seas.upenn.edu

### Authors

**Yiwei Qiang** − *Department of Mechanical Engineering and Applied Mechanics, University of Pennsylvania, Philadelphia, Pennsylvania 19104, United States*

**Sumukh S. Pande** − *Department of Materials Science and Engineering, University of Pennsylvania, Philadelphia, Pennsylvania 19104, United States*

Complete contact information is available at: https://pubs.acs.org/10.1021/acsnano.2c00471


### Author Contributions

Y.Q., S.S.P., D.L., and K.T.T. conceived the experiments. Y.Q. conducted the experiments. Y.Q., S.S.P., D.L., and K.T.T. analyzed the experimental results. D.L. and K.T.T. supervised the work. The manuscript was written through contributions of all authors. All authors have given approval to the final version of the manuscript.

### Notes

The authors declare no competing financial interest.

## ACKNOWLEDGMENTS

This work was supported by National Science Foundation via MRSEC DMR-1720530 and CMMI-1662695. Facilities support was provided by the Singh Center for Nanotechnology, part of the National Nanotechnology Coordinated Infrastructure Program, which is supported by the National Science Foundation grant NNCI-2025608. We thank Nissan Chemical America Corp. for supplying the Snowtex ST-YL and ST-ZL $SiO_2$ NP suspensions.

## REFERENCES


(1) Balazs, A. C.; Emrick, T.; Russell, T. P. Nanoparticle Polymer Composites: Where Two Small Worlds Meet. *Science* **2006**, *314*, 1107−1110.

(2) Harito, C.; Bavykin, D. V.; Yuliarto, B.; Dipojono, H. K.; Walsh, F. C. Polymer Nanocomposites Having a High Filler Content: Synthesis, Structures, Properties, and Applications. *Nanoscale* **2019**, *11*, 4653.

(3) Suresh, K.; Chowdhury, A.; Kumar, S. K.; Kumaraswamy, G. Critical Role of Processing on the Mechanical Properties of Cross-Linked Highly Loaded Nanocomposites. *Macromolecules* **2019**, *52*, 5955−5962.

(4) Sun, J.; Bhushan, B. Hierarchical Structure and Mechanical Properties of Nacre: A Review. *RSC Adv.* **2012**, *2*, 7617−7632.

(5) Zhao, H.; Yang, Z.; Guo, L. Nacre-Inspired Composites with Different Macroscopic Dimensions: Strategies for Improved Mechanical Performance and Applications. *NPG Asia Mater.* **2018**, *10*, 1−22.

(6) Wang, J.; Cheng, Q.; Tang, Z. Layered Nanocomposites Inspired by the Structure and Mechanical Properties of Nacre. *Chem. Soc. Rev.* **2012**, *41*, 1111−1129.

(7) Ding, F.; Liu, J.; Zeng, S.; Xia, Y.; Wells, K. M.; Nieh, M. P.; Sun, L. Biomimetic Nanocoatings with Exceptional Mechanical, Barrier, and Flame-Retardant Properties from Large-Scale One-Step Coassembly. *Sci. Adv.* **2017**, *3*, e1701212.

(8) Hoffmann, R.; Baric, V.; Naatz, H.; Schopf, S. O.; Mädler, L.; Hartwig, A. Inverse Nanocomposites Based on Indium Tin Oxide for Display Applications: Improved Electrical Conductivity via Polymer Addition. *ACS Appl. Nano Mater.* **2019**, *2*, 2273−2282.

(9) Zhu, H.; Li, Y.; Fang, Z.; Xu, J.; Cao, F.; Wan, J.; Preston, C.; Yang, B.; Hu, L. Highly Thermally Conductive Papers with Percolative Layered Boron Nitride Nanosheets. *ACS Nano* **2014**, *8*, 3606−3613.

(10) Joy, J.; George, E.; Haritha, P.; Thomas, S.; Anas, S. An Overview of Boron Nitride Based Polymer Nanocomposites. *J. Polym. Sci.* **2020**, *58*, 3115−3141.

(11) Wang, Z.; Fu, Y.; Meng, W.; Zhi, C. Solvent-Free Fabrication of Thermally Conductive Insulating Epoxy Composites with Boron Nitride Nanoplatelets as Fillers. *Nanoscale Res. Lett.* **2014**, *9*, 643.

(12) Cifra, P.; Benková, Z.; Bleha, T. Effect of Confinement on Properties of Stiff Biological Macromolecules. *Faraday Discuss.* **2008**, *139*, 377−392.

(13) Hsieh, C. C.; Doyle, P. S. Studying Confined Polymers Using Single-Molecule DNA Experiments. *Korea Aust. Rheol. J.* **2008**, *20*, 127−142.

(14) Sussman, D. M.; Tung, W. S.; Winey, K. I.; Schweizer, K. S.; Riggleman, R. A. Entanglement Reduction and Anisotropic Chain and Primitive Path Conformations in Polymer Melts under Thin Film and Cylindrical Confinement. *Macromolecules* **2014**, *47*, 6462−6472.

(15) Maguire, S. M.; Bilchak, C. R.; Corsi, J. S.; Welborn, S. S.; Tsaggaris, T.; Ford, J.; Detsi, E.; Fakhraai, Z.; Composto, R. J. Effect of Nanoscale Confinement on Polymer-Infiltrated Scaffold Metal Composites. *ACS Appl. Mater. Interfaces* **2021**, *13*, 44893−44903.

(16) Shin, K.; Obukhov, S.; Chen, J. T.; Huh, J.; Hwang, Y.; Mok, S.; Dobriyal, P.; Thiyagarajan, P.; Russell, T. P. Enhanced Mobility of Confined Polymers. *Nat. Mater.* **2007**, *6*, 961−965.

(17) García, N. A.; Barrat, J. L. Entanglement Reduction Induced by Geometrical Confinement in Polymer Thin Films. *Macromolecules* **2018**, *51*, 9850−9860.

(18) Rittigstein, P.; Priestley, R. D.; Broadbelt, L. J.; Torkelson, J. M. Model Polymer Nanocomposites Provide an Understanding of Confinement Effects in Real Nanocomposites. *Nat. Mater.* **2007**, *6*, 278−282.

(19) Napolitano, S.; Glynos, E.; Tito, N. B. Glass Transition of Polymers in Bulk, Confined Geometries, and near Interfaces. *Rep. Prog. Phys.* **2017**, *80*, No. 036602.

(20) Pye, J. E.; Roth, C. B. Above, below, and in-between the Two Glass Transitions of Ultrathin Free-Standing Polystyrene Films: Thermal Expansion Coefficient and Physical Aging. *J. Polym. Sci., Part B: Polym. Phys.* **2015**, *53*, 64−75.

(21) Lee, J. H.; Chung, J. Y.; Stafford, C. M. Effect of Confinement on Stiffness and Fracture of Thin Amorphous Polymer Films. *ACS Macro Lett.* **2012**, *1*, 122−126.

(22) Bay, R. K.; Shimomura, S.; Liu, Y.; Ilton, M.; Crosby, A. J. Confinement Effect on Strain Localizations in Glassy Polymer Films. *Macromolecules* **2018**, *51*, 3647−3653.

(23) Bay, R. K.; Zarybnicka, K.; Jančář, J.; Crosby, A. J. Mechanical Properties of Ultrathin Polymer Nanocomposites. *ACS Appl. Polym. Mater.* **2020**, *2*, 2220−2227.

(24) Genix, A. C.; Bocharova, V.; Kisliuk, A.; Carroll, B.; Zhao, S.; Oberdisse, J.; Sokolov, A. P. Enhancing the Mechanical Properties of Glassy Nanocomposites by Tuning Polymer Molecular Weight. *ACS Appl. Mater. Interfaces* **2018**, *10*, 33601−33610.

(25) Shao, C.; Keten, S. Stiffness Enhancement in Nacre-Inspired Nanocomposites Due to Nanoconfinement. *Sci. Rep.* **2015**, *5*, 16452.

(26) Galuska, L. A.; Muckley, E. S.; Cao, Z.; Ehlenberg, D. F.; Qian, Z.; Zhang, S.; Rondeau-Gagné, S.; Phan, M. D.; Ankner, J. F.; Ivanov, I. N.; Gu, X. SMART Transfer Method to Directly Compare the Mechanical Response of Water-Supported and Free-Standing Ultrathin Polymeric Films. *Nat. Commun.* **2021**, *12*, 2347.

(27) Kramer, E. J. Microscopic and Molecular Fundamentals of Crazing. In *Crazing in polymers*; Kausch, H. H., Ed.; Springer: Berlin, Heidelberg, 1983; pp 1−56.
(28) Alkhadra, M. A.; Root, S. E.; Hilby, K. M.; Rodriquez, D.; Sugiyama, F.; Lipomi, D. J. Quantifying the Fracture Behavior of Brittle and Ductile Thin Films of Semiconducting Polymers. *Chem. Mater.* **2017**, *29*, 10139−10149.
(29) Vogt, B. D. Mechanical and Viscoelastic Properties of Confined Amorphous Polymers. *J. Polym. Sci., Part B: Polym. Phys.* **2018**, *56*, 9−30.
(30) Lee, J. Y.; Crosby, A. J. Crazing in Glassy Block Copolymer Thin Films. *Macromolecules* **2005**, *38*, 9711−9717.
(31) Zhang, S.; Koizumi, M.; Cao, Z.; Mao, K. S.; Qian, Z.; Galuska, L. A.; Jin, L.; Gu, X. Directly Probing the Fracture Behavior of Ultrathin Polymeric Films. *ACS Polym. Au* **2021**, *1*, 16−29.
(32) Fu, Y.; Song, J. H. Large Deformation Mechanism of Glassy Polyethylene Polymer Nanocomposites: Coarse Grain Molecular Dynamics Study. *Comput. Mater. Sci.* **2015**, *96*, 485−494.
(33) Wang, H.; Hor, J. L.; Zhang, Y.; Liu, T.; Lee, D.; Fakhraai, Z. Dramatic Increase in Polymer Glass Transition Temperature under Extreme Nanoconfinement in Weakly Interacting Nanoparticle Films. *ACS Nano* **2018**, *12*, 5580−5587.
(34) Santagiuliana, G.; Picot, O. T.; Crespo, M.; Porwal, H.; Zhang, H.; Li, Y.; Rubini, L.; Colonna, S.; Fina, A.; Barbieri, E.; Spoelstra, A. B.; Mirabello, G.; Patterson, J. P.; Botto, L.; Pugno, N. M.; Peijs, T.; Bilotti, E. Breaking the Nanoparticle Loading-Dispersion Dichotomy in Polymer Nanocomposites with the Art of Croissant-Making. *ACS Nano* **2018**, *12*, 9040−9050.
(35) Huang, Y. R.; Jiang, Y.; Hor, J. L.; Gupta, R.; Zhang, L.; Stebe, K. J.; Feng, G.; Turner, K. T.; Lee, D. Polymer Nanocomposite Films with Extremely High Nanoparticle Loadings via Capillary Rise Infiltration (CaRI). *Nanoscale* **2015**, *7*, 798−805.
(36) Manohar, N.; Stebe, K. J.; Lee, D. Solvent-Driven Infiltration of Polymer (SIP) into Nanoparticle Packings. *ACS Macro Lett.* **2017**, *6*, 1104−1108.
(37) Venkatesh, R. B.; Han, S. H.; Lee, D. Patterning Polymer-Filled Nanoparticle Films via Leaching-Enabled Capillary Rise Infiltration (LeCaRI). *Nanoscale Horizons* **2019**, *4*, 933−939.
(38) Hor, J. L.; Jiang, Y.; Ring, D. J.; Riggleman, R. A.; Turner, K. T.; Lee, D. Nanoporous Polymer-Infiltrated Nanoparticle Films with Uniform or Graded Porosity via Undersaturated Capillary Rise Infiltration. *ACS Nano* **2017**, *11*, 3229−3236.
(39) Huang, X.; Zhi, C.; Jiang, P. Toward Effective Synergetic Effects from Graphene Nanoplatelets and Carbon Nanotubes on Thermal Conductivity of Ultrahigh Volume Fraction Nanocarbon Epoxy Composites. *J. Phys. Chem. C* **2012**, *116*, 23812−23820.
(40) Qiang, Y.; Turner, K. T.; Lee, D. Polymer-Infiltrated Nanoplatelet Films with Nacre-like Structure: Via Flow Coating and Capillary Rise Infiltration (CaRI). *Nanoscale* **2021**, *13*, 5545−5556.
(41) Venkatesh, R. B.; Manohar, N.; Qiang, Y.; Wang, H.; Tran, H. H.; Kim, B. Q.; Neuman, A.; Ren, T.; Fakhraai, Z.; Riggleman, R. A.; Stebe, K. J.; Turner, K.; Lee, D. Polymer-Infiltrated Nanoparticle Films Using Capillarity-Based Techniques: Toward Multifunctional Coatings and Membranes. *Annual Review of Chemical and Biomolecular Engineering.* **2021**, *12*, 411−437.
(42) Kim, B. Q.; Qiang, Y.; Turner, K. T.; Choi, S. Q.; Lee, D. Heterostructured Polymer-Infiltrated Nanoparticle Films with Cavities via Capillary Rise Infiltration. *Adv. Mater. Interfaces* **2021**, *8*, 2001421.
(43) Zeng, X.; Yang, K.; Yang, K.; Xu, S.; Xu, M.; Pi, P.; Wen, X. Robust Superhydrophobic Mesh with Excellent Chemical Resistance for Separation of Complicated Boiling Water/Oil Mixtures. *Mater. Res. Express* **2019**, *6*, No. 085025.
(44) Zeng, X.; Xu, S.; Pi, P.; Cheng, J.; Wang, L.; Wang, S.; Wen, X. Polymer-Infiltrated Approach to Produce Robust and Easy Repairable Superhydrophobic Mesh for High-Efficiency Oil/Water Separation. *J. Mater. Sci.* **2018**, *53*, 10554−10568.
(45) Zhang, J.; Zhang, L. Polystyrene/TiO2 Nanocomposite Coatings to Inhibit Corrosion of Aluminum Alloy 2024-T3. *ACS Appl. Nano Mater.* **2019**, *2*, 6368−6377.
(46) Bertei, A.; Nucci, B.; Nicolella, C. Effective Transport Properties in Random Packings of Spheres and Agglomerates. *Chem. Eng. Trans.* **2013**, *32*, 1531−1536.
(47) Hor, J. L.; Wang, H.; Fakhraai, Z.; Lee, D. Effect of Physical Nanoconfinement on the Viscosity of Unentangled Polymers during Capillary Rise Infiltration. *Macromolecules* **2018**, *51*, 5069−5078.
(48) Wang, H.; Qiang, Y.; Shamsabadi, A. A.; Mazumder, P.; Turner, K. T.; Lee, D.; Fakhraai, Z. Thermal Degradation of Polystyrene under Extreme Nanoconfinement. *ACS Macro Lett.* **2019**, *8*, 1413−1418.
(49) Hor, J. L.; Wang, H.; Fakhraai, Z.; Lee, D. Effects of Polymer-Nanoparticle Interactions on the Viscosity of Unentangled Polymers under Extreme Nanoconfinement during Capillary Rise Infiltration. *Soft Matter* **2018**, *14*, 2438−2446.
(50) Jiang, Y.; Hor, J. L.; Lee, D.; Turner, K. T. Toughening Nanoparticle Films via Polymer Infiltration and Confinement. *ACS Appl. Mater. Interfaces* **2018**, *10*, 44011−44017.
(51) Rubinstein, M.; Colby, R. H. Idea chains. In *Polymer physics*; Oxford university press: New York, 2003; pp 49−96.
(52) Wool, R. P. Rigidity Percolation Model of Polymer Fracture. *J. Polym. Sci., Part B: Polym. Phys.* **2005**, *43*, 168−183.
(53) Mikos, A. G.; Peppas, N. A. Polymer Chain Entanglements and Brittle Fracture. *J. Chem. Phys.* **1988**, *88*, 1337−1342.
(54) Pitman, G. L.; Ward, I. M. Effect of Molecular Weight on Craze Shape and Fracture Toughness in Polycarbonate. *Polymer* **1979**, *20*, 895−902.
(55) Lee, I.; Rolston, N.; Brunner, P. L.; Dauskardt, R. H. Hole-Transport Layer Molecular Weight and Doping Effects on Perovskite Solar Cell Efficiency and Mechanical Behavior. *ACS Appl. Mater. Interfaces* **2019**, *11*, 23757−23764.
(56) Choi, J.; Kim, W.; Kim, D.; Kim, S.; Chae, J.; Choi, S. Q.; Kim, F. S.; Kim, T. S.; Kim, B. J. Importance of Critical Molecular Weight of Semicrystalline N-Type Polymers for Mechanically Robust, Efficient Electroactive Thin Films. *Chem. Mater.* **2019**, *31*, 3163−3173.
(57) Lin, E. Y.; Frischknecht, A. L.; Riggleman, R. A. Chain and Segmental Dynamics in Polymer−Nanoparticle Composites with High Nanoparticle Loading. *Macromolecules* **2021**, *54*, 5335−5343.
(58) Schneider, G. J.; Nusser, K.; Willner, L.; Falus, P.; Richter, D. Dynamics of Entangled Chains in Polymer Nanocomposites. *Macromolecules* **2011**, *44*, 5857−5860.
(59) Li, Y.; Kröger, M.; Liu, W. K. Nanoparticle Effect on the Dynamics of Polymer Chains and Their Entanglement Network. *Phys. Rev. Lett.* **2012**, *109*, 118001.
(60) De Gennes, P. G. Polymer Solutions in Good Solvents. In *Scaling Concepts in Polymer Physics*; Cornell University Press: Ithaca and London, 1979: pp 69−97.
(61) Isaacson, S. G.; Lionti, K.; Volksen, W.; Magbitang, T. P.; Matsuda, Y.; Dauskardt, R. H.; Dubois, G. Fundamental Limits of Material Toughening in Molecularly Confined Polymers. *Nat. Mater.* **2016**, *15*, 294−298.
(62) Wang, C.; Isaacson, S. G.; Wang, Y.; Lionti, K.; Volksen, W.; Magbitang, T. P.; Chowdhury, M.; Priestley, R. D.; Dubois, G.; Dauskardt, R. H. Surface Chemical Functionalization to Achieve Extreme Levels of Molecular Confinement in Hybrid Nanocomposites. *Adv. Funct. Mater.* **2019**, *29*, 1903132.
(63) Isaacson, S. G.; Matsuda, Y.; Lionti, K.; Frot, T.; Volksen, W.; Dauskardt, R. H.; Dubois, G. Using Unentangled Oligomers to Toughen Materials. *ACS Appl. Mater. Interfaces* **2018**, *10*, 27549−27554.
(64) Fleck, N. A.; Hutchinson, J. W.; Zhigang, S. Crack Path Selection in a Brittle Adhesive Layer. *Int. J. Solids Struct.* **1991**, *27*, 1683−1703.
(65) Lin, E. Y.; Frischknecht, A. L.; Riggleman, R. A. Origin of Mechanical Enhancement in Polymer Nanoparticle (NP) Composites with Ultrahigh NP Loading. *Macromolecules* **2020**, *53*, 2976.


https://doi.org/10.1021/acsnano.2c00471
*ACS Nano* 2022, 16, 6372−6381

(66) Pressly, J. F.; Riggleman, R. A.; Winey, K. I. Polymer Diffusion Is Fastest at Intermediate Levels of Cylindrical Confinement. *Macromolecules* **2018**, *51*, 9789−9797.
(67) An, L.; Zhang, D.; Zhang, L.; Feng, G. Effect of Nanoparticle Size on the Mechanical Properties of Nanoparticle Assemblies. *Nanoscale* **2019**, *11*, 9563−9573.
(68) Leroch, S.; Wendland, M. Influence of Capillary Bridge Formation onto the Silica Nanoparticle Interaction Studied by Grand Canonical Monte Carlo Simulations. *Langmuir* **2013**, *29*, 12410−12420.
(69) Lee, D.; Gemici, Z.; Rubner, M. F.; Cohen, R. E. Multilayers of Oppositely Charged SiO2 Nanoparticles: Effect of Surface Charge on Multilayer Assembly. *Langmuir* **2007**, *23*, 8833−8837.
(70) Lagström, T.; Gmür, T. A.; Quaroni, L.; Goel, A.; Brown, M. A. Surface Vibrational Structure of Colloidal Silica and Its Direct Correlation with Surface Charge Density. *Langmuir* **2015**, *31*, 3621−3626.
(71) Lee, I.; Kim, S.; Yun, J.; Park, I.; Kim, T.-S. Interfacial Toughening of Solution Processed Ag Nanoparticle Thin Films by Organic Residuals. *Nanotechnology* **2012**, *23*, 485704.
(72) Kanninen, M. F. An Augmented Double Cantilever Beam Model for Studying Crack Propagation and Arrest. *Int. J. Fract.* **1973**, *9*, 83−92.





https://doi.org/10.1021/acsnano.2c00471
*ACS Nano* 2022, 16, 6372−6381